Journal of Power Sources 251 (2014) 386–392

Contents lists available at ScienceDirect

Journal of Power Sources

journal homepage: www.elsevier.com/locate/jpowsour

Nano $LiFePO_4$ in reduced graphene oxide framework for efficient high-rate lithium storage

Junyoung Mun [a], Hyung-Wook Ha [b], Wonchang Choi [c,*]

[a] Department of Energy and Chemical Engineering, Incheon National University, 12-1, Songdo-dong, Yeonsu-gu, Incheon 406-840, Republic of Korea
[b] Energy Division, CSelsolar, 176, Galmachi-ro, Jungwon-gu, Seongnam-si, Gyeonggi-do 462-120, Republic of Korea
[c] Center for Energy Convergence, Korea Institute of Science and Technology, Hwarangno 14-gil 5, Seongbuk-gu, Seoul 136-791, Republic of Korea

HIGHLIGHTS

- A composite containing reduced graphene oxide within nano $LiFePO_4$ is proposed.
- The composite has an effective electron pathway and a highly meso-porous structure.
- The composite shows superior rate capabilities.

GRAPHICAL ABSTRACT

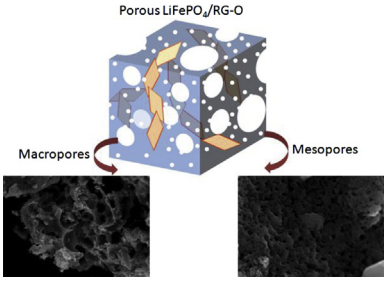

ARTICLE INFO

Article history:
Received 24 September 2013
Received in revised form
14 November 2013
Accepted 16 November 2013
Available online 4 December 2013

Keywords:
Reduced graphene oxide
Lithium-ion batteries
Cathode material
Lithium iron phosphate
Sol–gel method

ABSTRACT

In this paper, we report a simple sol–gel method for the synthesis of a composite containing reduced graphene oxide (R-GO) embedded within nano $LiFePO_4$ particles for a lithium-ion battery cathode. This composite has an effective electron pathway and a highly meso-porous structure as compared to conventional $LiFePO_4$. Highly conductive R-GO, together with the meso-porosity results in a material that has good electronic conductivity and high electrolyte permeability. Electrodes fabricated from the composite exhibited excellent performance when evaluated as lithium-ion battery cathodes, including compared to pristine $LiFePO_4$. The electrode of the R-GO composite exhibits excellent rate capabilities of 125 mAh g^{-1} at 10 C, whereas pristine $LiFePO_4$ could deliver only 81.5 mAh g^{-1} at the same condition. It also achieves an improved cyclability with capacity retention ratios of 92.48% after 200 cycles at 10 C, as well.

1. Introduction

Since rechargeable lithium-ion batteries were firstly commercialized by SONY on 1991, they have become the main power source for mobile electronics and telecommunication devices [1]. Meeting the demands of emerging and future applications of electrical energy storage, such as electric vehicles, requires electrode materials with improved energy densities and high-rate capabilities. Since its discovery by Padhi et al. [2], lithium iron phosphate ($LiFePO_4$) olivine has been widely recognized as a promising cathode material for the replacement of commonly-used lithium cobalt oxide ($LiCoO_2$). This is due to its high theoretical capacity (170 mAh g^{-1}), advantageous environmental properties (Co is toxic), and low cost (Fe is abundant). Furthermore, $LiFePO_4$ exhibits excellent cyclability (the availability of a single-phase transformation pathway of lithiation and de-lithiation because $LiFePO_4$

* Corresponding author. Tel.: +82 2 958 5253; fax: +82 2 958 5229.
E-mail addresses: wonchangchoi@kist.re.kr, unchaeng@gmail.com (W. Choi).

0378-7753/$ – see front matter © 2013 Elsevier B.V. All rights reserved.
http://dx.doi.org/10.1016/j.jpowsour.2013.11.034

and $FePO_4$ are isostructural) and has excellent thermal stability compared to other layered structure cathode materials owing to robust structure of PO_4^-, even when fully charged [3].

Despite these benefits, the commercialization of $LiFePO_4$ is currently hindered by drawbacks such as low values of electronic conductivity (*ca.* 10^{-9}–10^{-10} S cm^{-1}) [4] and Li^+ diffusivity (10^{-14}–10^{-16} cm^2 s^{-1}) [5]. Such disadvantages are particularly detrimental towards high-rate operation. Previous efforts to overcome these barriers have focused on the use of alternative material morphologies [6] and synthetic routes [7–9]. For example, conductivity was enhanced (up to 10^{-3} S m^{-1}) through the non-stoichiometric doping of $LiFePO_4$ with metal supervalent cations of magnesium, zirconium, titanium, niobium, and tungsten [4,10]. Although effective, dopant incorporation into Li^+ sites may cause reduced capacity [11]. An alternative route towards improved conductivity has been to coat $LiFePO_4$ electrodes with materials such as carbon [12–16], ruthenium dioxide [17,18], and conducting polymers [19,20]. Elsewhere, Li^+ diffusivity was improved through control of $LiFePO_4$ particle size [21].

Recently, reduced graphene oxide (R-GO), a chemically-produced analog of graphene, has been used extensively as a performance-enhancing additive for many electrical energy storage electrode materials. This has included materials used as both anodes and cathodes in lithium-ion batteries. The usefulness of R-GO in this respect is due to several unique properties, such as a high specific surface area (theoretically up to 2630 m^2 g^{-1}), good electronic conductivity, and superior mechanical characteristics. Composites of $LiFePO_4$ and R-GO have previously been synthesized using co-precipitation, spray drying and hydrothermal methods, with the materials produced enabling discharge capacities as high as 160 mAh g^{-1} at a 0.2 C rate (1 C being the current density required to fully charge the battery in one hour) [22–24]. Here, we report the production of a composite of $LiFePO_4$ and R-GO (herein $LiFePO_4$/R-GO) using a simple method based on the sol–gel technique. Multiple material characterizations reveal that this method leads to the production of a hierarchically porous structure comprised of R-GO platelets embedded within aggregated $LiFePO_4$ particles 40–50 nm in size. During charge/discharge testing, electrodes fabricated from this $LiFePO_4$/R-GO composite displayed excellent performance with respect to discharge capacity, capacity retention during cycling, and coulombic efficiency, including compared to pristine $LiFePO_4$ (produced using the same sol–gel method) and at high rates of 10 C.

Indeed, what strongly differentiates the work reported here from others involving $LiFePO_4$ and R-GO is the high rate discharge capacity of the porous $LiFePO_4$/R-GO composite formed. For example, our material yields a value of 125 mAh g^{-1} at a rate of 10 C, compared to 109 mAh g^{-1} at 10 C for material prepared by a co-precipitation method [22], or 81.5 mAh g^{-1} for material prepared hydrothermally [23].

2. Experimental

2.1. Sample preparation

Graphite oxide was synthesized using a modified Hummers method from natural graphite (SP-1, Bay Carbon, Inc.) [25]. Exfoliation of graphite oxide to a stable dispersion of graphene oxide (G-O) platelets was achieved by ultrasonication in deionized water (18 MΩ resistance) for 1 h. The concentration of G-O dispersions with respect to the mass of graphite oxide added was 1 g L^{-1}. $LiFePO_4$/R-GO composites were prepared using a sol–gel method. First, 0.03 mol of lithium dihydrogen phosphate (LiH_2PO_4, Sigma–Aldrich) was dissolved in 200 mL of water and stirred at 70 °C for 1 h. Second, 0.03 mol of iron (III) chloride (Acros) and 0.03 mol of ammonium citrate (Sigma–Aldrich) were dissolved in 300 mL of G-O dispersion by ultrasonication for 30 min followed by vigorous stirring at 65 °C for 1 h. The two solutions were mixed together and then dried at 70 °C for 24 h. The dry material was ground using a mortar and pestle and then calcined inside a tube furnace in an atmosphere of argon (95 vol%) and hydrogen (5 vol%). Calcination involved heating the material at a rate of 10 °C min^{-1} from room temperature to 700 °C, and holding at this temperature for 10 h. Pristine $LiFePO_4$ was produced using an identical procedure, except 300 mL water was used instead of dispersed G-O.

2.2. Materials characterization

Powder XRD was carried out using a Philips X'Pert PRO with Cu Kα radiation ($\lambda = 1.5404$ Å). TGA was conducted over a temperature range of 40–600 °C, at a heating rate of 3 °C min^{-1}, and under dry air, using a 4000/Perkin–Elmer thermogravimetric analyzer. A JEOL 2010F was used for TEM studies. SEM was carried out using a Hitachi S-5500. The accelerating voltages for TEM and SEM were 200 kV and 20 kV, respectively. Raman measurements were made using a WiTec Alpha300 confocal Raman microscope with a 532 nm excitation source from a frequency-doubled Nd:Yag laser. Nitrogen adsorption measurements (BET, Micromeritics Tristar 3000) were carried out at 77 K.

2.3. Electrode fabrication and electrochemical testing

Electrodes were fabricated by mixing 80 wt.% active material (*i.e.*, $LiFePO_4$/R-GO or pristine $LiFePO_4$) with 15 wt.% acetylene black (Alfa Aesar) and 5 wt.% polytetrafluoroethylene (PTFE; Sigma–Aldrich). The components were mixed together, rolled into thin sheets, and punched to form discs of area ~0.71 cm^2. Typically, each electrode had an active material content of ~4 mg. Following their construction, electrodes were dried under vacuum at 120 °C for longer than 12 h. For testing, electrodes were assembled into CR2032 coin cells in an argon-filled glovebox. At least, three coin cells were assembled to confirm the behavior of the prepared samples. A solution of 1 M $LiPF_6$ in 1:1 (v/v) ethylene carbonate/diethyl carbonate (EC:DEC; Novolyte Ltd.) was employed as the electrolyte. A Teflon membrane (#2400, Celgard), and Li ribbon (Sigma–Aldrich) were used as the separator and anode, respectively. Galvanostatic charge/discharge tests were carried out using a LAND CT2001 cell tester in the potential range of 4.5–2.5 V (*vs.* Li/Li^+). In all cases, current densities were calculated with respect to the total mass of active material. Impedance measurements (amplitude 5 mV, frequencies in the range 100 kHz–0.01 Hz) were carried out on fully discharged cells after galvanostatically cycling 50 times (to ensure that the cathode solid electrolyte interface layer was fully developed and stable). The lithium ion diffusion coefficient of the prepared electrodes were calculated by using Warburg factors [26]. All electrochemical testing was carried out at room temperature.

3. Results and discussion

3.1. Materials characterization

The sol–gel method used for the production of the $LiFePO_4$/R-GO composite is detailed in the Experimental section. The method involves the simple mixing of $LiFePO_4$ precursors with a G-O dispersion. The mixture formed is dried to give a solid that is then calcined at 700 °C under Ar and H_2 filled environment. During the calcination, the G-O is thermally reduced to R-GO [27,28]. After synthesis, the proportions of amorphous carbon and R-GO in the composite were determined by TGA, as 20.7 wt.% and 5.04 wt.%,

respectively (Fig. 1). The remaining 20.7 wt.% is attributed to the presence of amorphous carbon formed from the thermal decomposition of ammonium citrate that is used during the sol–gel process under the reductive condition. Pristine LiFePO4 was produced using the same method, but without the addition of G-O.

Following materials synthesis, the crystal structures were identified by using X-ray diffraction (XRD). Fig. 2a and b is XRD patterns of the $LiFePO_4$/R-GO composite and pristine $LiFePO_4$, respectively. For both diffractograms, analysis of the diffraction peaks indicates the existence of $LiFePO_4$ with an olivine structure (JCPDS # 83-2092), indexed as orthorhombic with the space group *Pnma*, (the theoretical XRD pattern for such a structure is provided, for comparison, in Fig. 2d). It has been calculated that the particle size of the crystals present based on the full-width at half-maximum (FWHM) of the major diffraction peaks associated with (020), (011), and (131), together with the Scherrer equation, shown below.

$$t = 0.9\lambda/B\cos\theta \quad (1)$$

where, t is the crystallite size, λ is the wavelength of the X-ray, B is the FWHM of the XRD peaks, and θ is the Bragg angle. On the basis of this equation, the crystallite sizes of the pristine $LiFePO_4$ and $LiFePO_4$/R-GO composite materials were determined as 86 and 39 nm, respectively [29]. No impurity-related peaks are visible in the XRD data for either material. The principle difference in the two diffractograms is the presence of a broad feature spanning 2θ values between 20° and 35° in the pattern for the composite. This feature can be assigned to diffraction from interlayer separations in R-GO, being also observed in XRD patterns of 'papers' made from hydrazine-reduced G-O [30], as shown in Fig. 2c. The feature is centered at a 2θ value of ~25° indicating an interlayer spacing of about 0.36 nm, which is slightly higher than that of well-ordered graphite. The relative broadness of this R-GO peak compared to that of graphite can be attributed to increased disorder in the through-plane direction and smaller platelet sizes caused by the use of sonication.

Further material analysis was carried out using Raman spectroscopy. Fig. 3a and b is Raman spectra of the $LiFePO_4$/R-GO composite and pristine $LiFePO_4$, respectively. Each spectrum contains a broad band centered at ~950 cm^{-1}, attributable to the symmetric PO_4^{3-} intramolecular stretching vibration of $LiFePO_4$

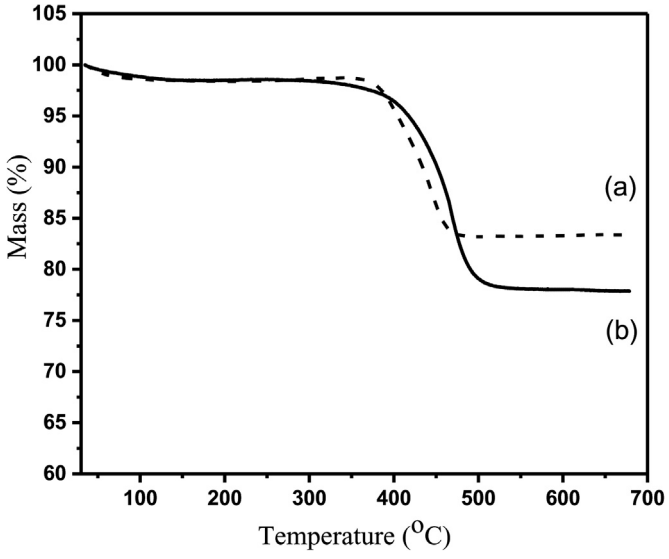

Fig. 1. TGA curves of (a) pristine $LiFePO_4$, and (b) $LiFePO_4$/R-GO composite in the temperature range 35–700 °C at a heating rate of 3 °C min^{-1} in dry air.

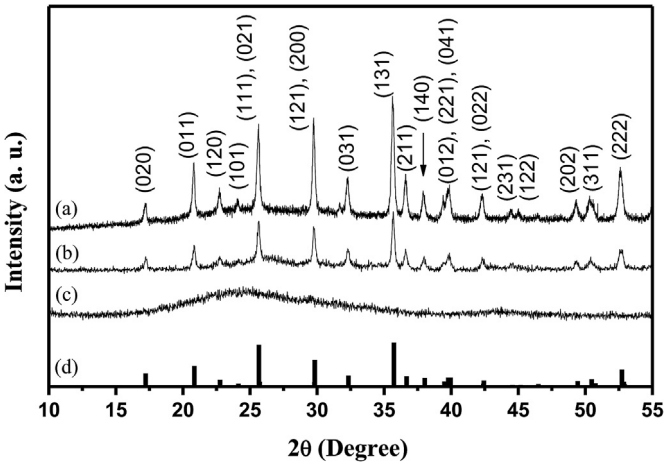

Fig. 2. XRD patterns of (a) $LiFePO_4$/R-GO composite material, (b) pristine $LiFePO_4$, (c) R-GO and (d) JCPDS # 83-2092.

[31]. In addition, the spectrum in Fig. 3a contains a broad peak at 1584 cm^{-1}. This feature is the so-called G-band and is indicative of bond stretching of sp^2-hybridized aromatic rings and chain carbon frameworks, which are found within R-GO platelets. Also attributable to R-GO, and visible in the same spectrum, is a prominent peak at 1352 cm^{-1}. This peak is known as the disorder-induced phonon mode (the D-band) and is commonly seen in Raman spectra of carbon materials having a disordered structure. As shown in Fig. 3b, D and G bands were also observed in the Raman spectra of pristine $LiFePO_4$. We attribute this result to the presence of amorphous carbon introduced during the sol–gel process, as discussed above. After thermal reduction of G-O at 700 °C, as compared with pristine $LiFePO_4$, the D/G intensity ratio (i.e., D peak intensity/G peak intensity) of the $LiFePO_4$/R-GO composite increases owing to lack of stacked graphene layers of the R-GO like graphite. This is consistent with previous Raman spectra of R-GO [32,33].

The morphologies of the materials were determined using electron microscopy, both scanning (SEM) and transmission (TEM). First, we consider the $LiFePO_4$/R-GO composite, representative images of which are shown in Fig. 4a–c. The SEM images in Fig. 4a and b indicates that this material is formed as large secondary particles several microns in size. The surfaces of these particles are seen to contain numerous large micron sized pores and also openings of channels that run into particle interiors. These openings have diameters of 10–20 nm. Their presence is also supported by pore size distribution data (Fig. S1). TEM allowed closer inspection of the material. Fig. 4c shows a TEM image that reveals aggregated $LiFePO_4$ primary particles, 40–50 nm in size, that make intimate contact with R-GO platelet surfaces which are observed as a wrinkled morphology (inset of Fig. 4c). This result is highly correspondent with XRD result in Fig. 1.

Fig. 4d is a schematic of the $LiFePO_4$/R-GO composite material, which indicates how the close packing and irregular shapes of the $LiFePO_4$ particles results in the formation of a mesoporous structure. Thus, the composite is hierarchically porous, containing a network of mesopores and larger channels. Such mesoporous structures have been shown previously to provide enhanced electrolyte–electrode contacts, resulting in fast Li ion mobility and lower charge-transfer resistance [34].

Fig. 4e and f is typical SEM and TEM images of the pristine $LiFePO_4$ material, respectively. It is obvious that, without the presence of R-GO, pristine $LiFePO_4$ particles were irregular shape formed at the same synthetic condition, indicating that the R-GO plays an important role in the formation of $LiFePO_4$ nanoparticles.

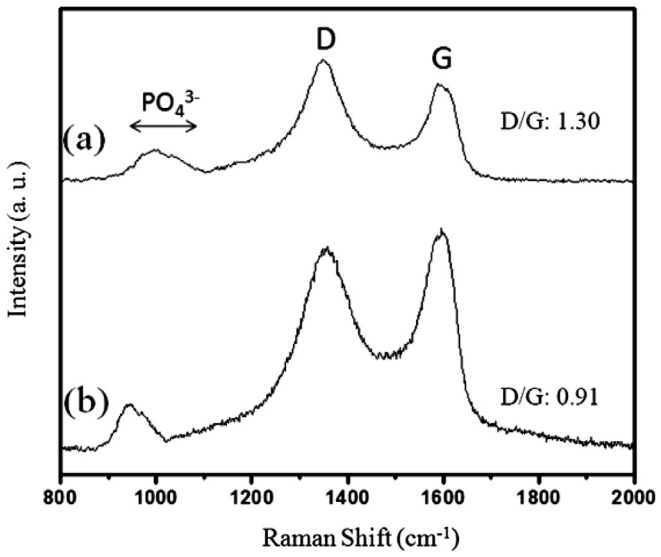

Fig. 3. Raman spectra of (a) $LiFePO_4$/R-GO composite and (b) pristine $LiFePO_4$ materials, respectively.

SEM analysis revealed that this pristine material is formed as irregular shape particles. These particles were observed to be covered with carbon. As before, this carbon is attributed to the thermal decomposition of the citrate-containing starting gel. However, the obtained amorphous carbon was not highly electronic conductive like R-GO, resulting in insufficient electronic conduction pathway and therefore allowing for only limited enhancement of rate performance. Further differences on smaller scales were revealed by TEM. Notably, the pristine material was seen to contain aggregated $LiFePO_4$ particles with individual primary particle sizes in the range 80–90 nm, significantly larger than those seen in $LiFePO_4$/R-GO.

Further details regarding material porosities were obtained through nitrogen adsorption measurements. Adsorption isotherms of both $LiFePO_4$/R-GO composite and pristine $LiFePO_4$ materials exhibited typical Brunauer, Deming, Deming, and Teller (BDDT) type IV shapes with H3-type hysteresis loops, according to IUPAC classifications [35]. Such features are indicative of open slit-shaped capillaries. Brunauer–Emmett–Teller (BET) analysis revealed similar specific surface areas of 77 $m^2\ g^{-1}$ and 68 $m^2\ g^{-1}$ and pore volumes of 0.19 $cm^3\ g^{-1}$ and 0.12 $cm^3\ g^{-1}$ for the composite and pristine materials, respectively. The higher value for the former could be due to the smaller $LiFePO_4$ particles present. The difference between the prepared samples was small, therefore it was hard to imagine that those surface characteristics influenced the electrode fabrication process relating the effect of conducting agent and binder. Barret–Joyner–Halenda (BJH) analysis, based on the Kelvin equation and corrected for multilayer adsorption, indicated the presence of mesopores of average diameter ~10 nm in both materials (see Supporting information, Fig. S1).

3.2. Electrochemical performance

The fabrication of electrodes from the $LiFePO_4$/R-GO composite and pristine $LiFePO_4$ materials involved the mixing of each material with acetylene black and PTFE (see the Experimental section for details), as is commonplace.

Fig. 5 presents the charge/discharge voltage profiles acquired using these electrodes. In each case, the current rate was 0.2 C. These profiles show that the composite material is associated with a wider voltage plateau at 3.4 V than that of the pristine $LiFePO_4$. As a result of this wider plateau, the $LiFePO_4$/R-GO electrode provided a larger discharge capacity of 152 mAh g^{-1} than the pristine material (138 mAh g^{-1}). Furthermore, there was a smaller polarization between the charge and discharge plateaus for the composite (50 mV, compared to 60 mV for the pristine material), suggesting that lithiation/delithiation reaction kinetics resistances are relieved in the composite [17]. Reduced resistances might be due to the presence of conductive R-GO, which acts to enhance electron transfer between the external circuit and $LiFePO_4$. In addition, the presence of channels and smaller sized $LiFePO_4$ particles may allow for improved Li^+ accessibility to greater proportions of active material.

To further investigate electrode kinetics, discharge capacities were studied as a function of rate. Fig. 6 contains plots of discharge capacity against rate, for rates in the range of 0.2–5 C. As mentioned above, at low rates of 0.2 C, the $LiFePO_4$/R-GO electrode displayed a discharge capacity of 152 mAh g^{-1}, about 10% higher than that measured using the $LiFePO_4$ electrode. Importantly, the $LiFePO_4$/R-GO electrode continued to exhibit good performance at elevated rates. For example, at the highest rate of 5 C, the voltage plateau of this electrode remained at 3.4 V (see Supporting

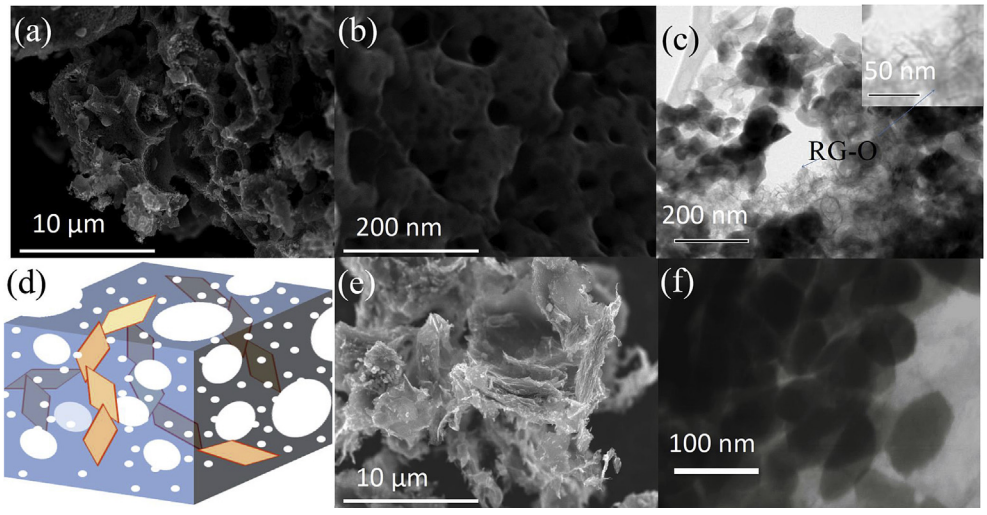

Fig. 4. (a, b) SEM images at different magnifications and (c) TEM image (inset: R-GO); (d) schematic illustration of porous $LiFePO_4$/R-GO composite; (e) SEM and (f) TEM of pristine $LiFePO_4$ material.

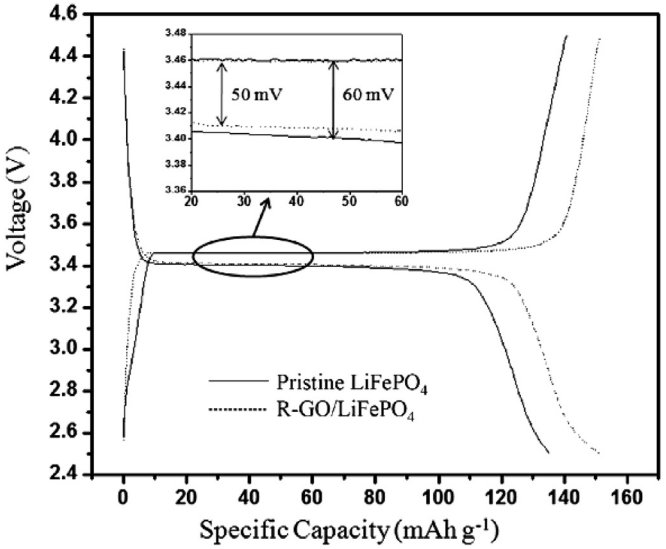

Fig. 5. The 1st charge/discharge voltage profiles of pristine $LiFePO_4$ (solid line) and $LiFePO_4$/R-GO composite (dotted line) at a current density of 0.2 C. Inset: the circled region, enlarged.

information, Fig. S2) while the discharge capacity was 135 mAh g^{-1}. This discharge capacity is 88% of that measured at a rate of 0.2 C and 51% greater than that exhibited by the $LiFePO_4$ electrode. It is also similar to that of the pristine electrode acquired using the lowest rate of 0.2 C. Moreover, when the rate was returned to 0.2 C after 38 cycles at successively higher rates, the $LiFePO_4$/R-GO electrode recovered most of its original capacity (150 mAh g^{-1} for the 40th cycle), while the pristine $LiFePO_4$ electrode did not.

Fig. 7a and b shows the cycling performance of the electrodes, measured at a rate of 0.2 and 10 C, respectively. For all cycles at each rate, the $LiFePO_4$/R-GO electrode showed much higher capacity than the pristine $LiFePO_4$ electrode, demonstrating the benefit of introducing highly conductive R-GO. After 50 cycles at a low current rate of 0.2 C, the $LiFePO_4$/R-GO and pristine $LiFePO_4$ electrodes deliver approximately 99% and 98% of the initial capacity, respectively, while the coulombic efficiency of both electrodes (calculated as discharge capacity/charge capacity) remains close to 100% (see Supporting information, Fig. S3). At higher rates of 10 C, the remarkable electrochemical characteristics of the $LiFePO_4$/R-GO

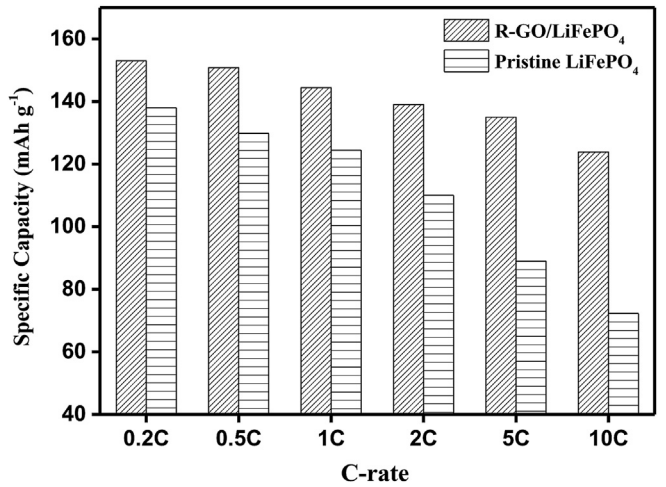

Fig. 6. Rate capability of pristine $LiFePO_4$ (closed circles) and $LiFePO_4$/R-GO (open circles) composite electrode at various current densities.

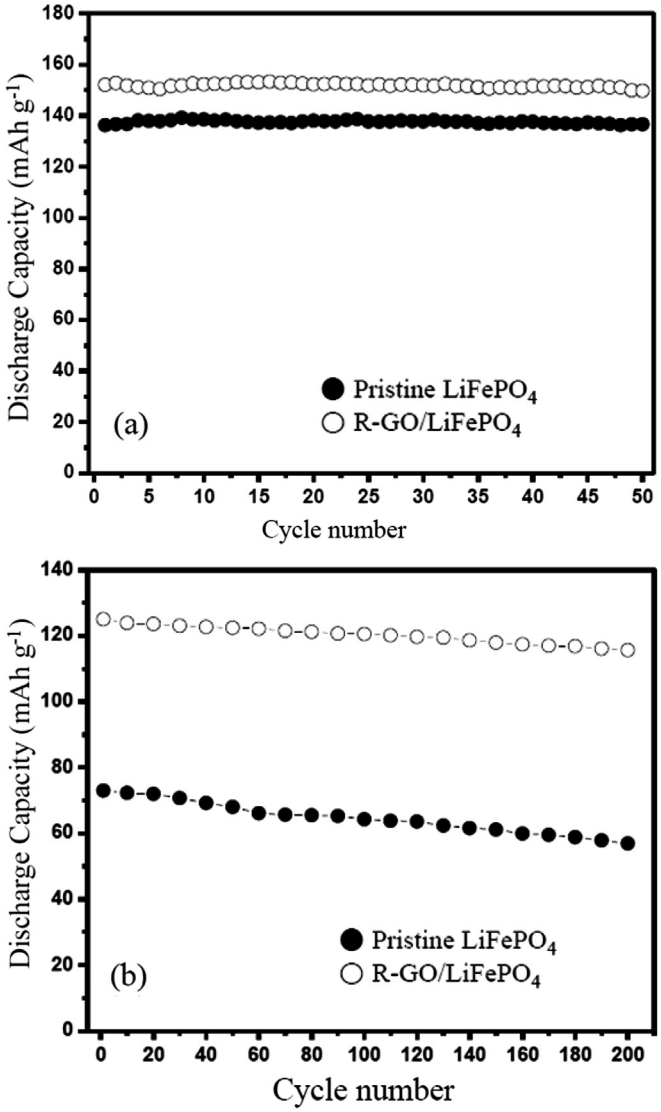

Fig. 7. Dependence of discharge capacity on cycle number for the pristine $LiFePO_4$ (closed circles) and $LiFePO_4$/R-GO (open circles) composite at a 0.2 C (a) and 10 C (b) rate, respectively.

composite during long-term cycling (200 cycles) are even clearer, with the $LiFePO_4$/R-GO composite retaining a discharge capacity of 125 mAh g^{-1} in contrast to just 73 mAh g^{-1} for the pristine $LiFePO_4$ Furthermore, the $LiFePO_4$/R-GO electrode at a high current rate of 10 C shows a much higher discharge capacity than previously reported porous $LiFePO_4$ and carbon composite using a different synthetic method [36–39], and of another $LiFePO_4$/R-GO composite [22,23].

Taking into account the cyclability of the materials, we note that the $LiFePO_4$/R-GO composite electrode shows remarkable electrochemical cycling stability with less than 6% decay in discharge capacity (better than 94% retention) up to 200 cycles despite the depth of charge and discharge of $LiFePO_4$/R-GO composite is higher than those of the pristine $LiFePO_4$. The pristine $LiFePO_4$ electrode material had only 78% capacitance retention after 200 cycles. It should be noted that the electrochemical performance of $LiFePO_4$ is influenced by the quality of the carbon coating [11]. Although many studies have investigated the contribution of residual amorphous carbons to electrochemical performance, the superior electrochemical performance of the $LiFePO_4$/R-GO electrode can be

explained that R-GO platelets in the composite have a good electrical conductivity and provide highly porous channels between $LiFePO_4$ nanoparticles as well as the possible connection between residual amorphous carbons, which decrease the resistance of electrodes.

Electrochemical impedance spectroscopy was used to investigate charge transfer resistance. Fig. 8 displays Nyquist plots for both electrodes. An intercept at the Z' real axis in the high frequency region corresponds to electrolyte resistance, R_s, in the equivalent circuits. The semicircle in the intermediate frequency range indicates the charge transfer resistance, R_{ct}, which is related to both the charge transfer through and the double-layer capacitance at the electrode/electrolyte interface. The shapes of the semicircles provide information pertaining to the charge-transfer resistances of the electrochemical reactions taking place [40,41]. Of particular note is that the semicircle obtained from the $LiFePO_4$/R-GO electrode has a significantly smaller diameter than that of the pristine material. Thus, it can be seen that R_{ct} decreased dramatically from 50 Ω for the pristine $LiFePO_4$ to 25 Ω with the introduction of approximately 5 wt.% R-GO. This result is consistent with the aforementioned larger discharge capacity and improved rate capability.

Based on the AC impedance analyses, the lithium diffusion coefficient could be calculated by using Warburg factor and the Equation (2) [42].

$$D = 0.5R^2T^2A^{-2}F^4C^2\sigma^2 \quad (2)$$

R is the gas constant, T is the temperature, A is the electrode surface area of the cathode electrode, F is the Faraday constant, C is the concentration of lithium ion and σ is the Warburg factor obtained from the slope for $\omega^{-0.5}$ (angular velocity) and Z′ (real part of impedance). The lithium diffusion coefficient for the pristine $LiFePO_4$ and $LiFePO_4$/R-GO were 4.7×10^{-14} cm^2 s^{-2} and 2.2×10^{-13} cm^2 s^{-2}, respectively. The $LiFePO_4$/R-GO exhibited the improved lithium conductivity which highly influenced rate capabilities. In Fig. S1, the particle sizes of $LiFePO_4$ in both samples were similar and nano-scale. Judging from this, it was hard to believe that the improved rate capabilities were influenced by the only lithium diffusivities. It is rational that the electronic conductivity was greatly improved by introducing the R-GO matrix into LiFePO4 powder, leading to high rate capability and low polarization of the electrode. Both the increased lithium diffusion coefficient and the improved electronic conductivity affected the rate capability.

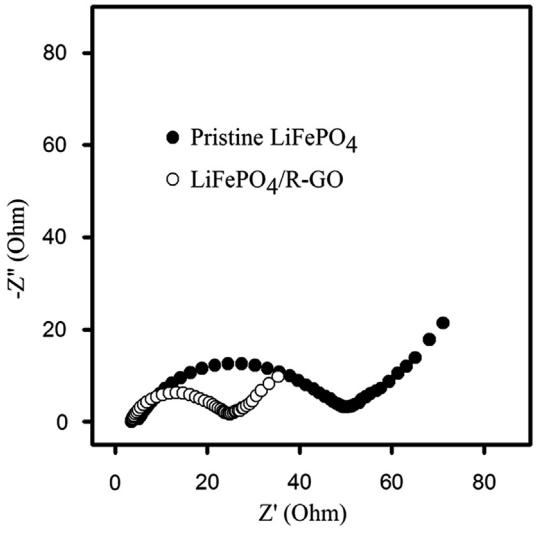

Fig. 8. AC impedance spectroscopy of pristine $LiFePO_4$ (closed circles) and $LiFePO_4$/R-GO composite (open circles) electrodes.

4. Conclusion

In summary, a simple method based on the sol–gel approach has been established for the synthesis of a composite of $LiFePO_4$ and R-GO platelets. Many studies have investigated the contribution of residual amorphous carbons to the electrochemical performance of $LiFePO_4$. Here, we attribute the superior performance of the $LiFePO_4$/R-GO electrode to the presence of the R-GO platelets, which improve electrical conductivity and provide highly porous channels between $LiFePO_4$ nanoparticles, enhancing electron transport and allowing the electrolyte to penetrate deep into the electrode material thereby reducing the Li^+ ion transport length. As a result of these characteristics, electrodes fabricated from the $LiFePO_4$/R-GO composite exhibit excellent performance when tested as lithium ion battery cathodes in comparison to those produced without R-GO, including at high rates of up to 10 C. As such, cathodes fabricated from this composite are promising for high power electrical energy-storage applications such as electric vehicles and power tools.

Acknowledgments

This work was supported by the National Research Foundation of Korea Grant funded by the Korean Government (MEST) (NRF-2010-C1AAA001-2010-0028958).

Appendix A. Supplementary data

Supplementary data related to this article can be found at http://dx.doi.org/10.1016/j.jpowsour.2013.11.034.

References

[1] K. Kang, Y.S. Meng, J. Breger, C.P. Grey, G. Ceder, Science 311 (2006) 977–980.
[2] A.K. Padhi, K.S. Nanjundaswamy, J.B. Goodenough, J. Electrochem. Soc 144 (1997) 1188–1194.
[3] J. Jiang, J.R. Dahn, Electrochem. Commun. 6 (2004) 39–43.
[4] S.-Y. Chung, Y.-M. Chiang, Electrochem. Solid-State Lett. 6 (2003) A278–A281.
[5] P.P. Prosini, M. Lisi, D. Zane, M. Pasquali, Solid State Ionics 148 (2002) 45–51.
[6] S. Lim, C.S. Yoon, J. Cho, Chem. Mater. 20 (2008) 4560–4564.
[7] C. Delacourt, P. Poizot, J.-M. Tarascon, C. Masquelier, Nat. Mater. 4 (2005) 254–260.
[8] X.-Z. Liao, Z.-F. Ma, Y.-S. He, X.-M. Zhang, L. Wang, Y. Jiang, J. Electrochem. Soc 152 (2005) A1969–A1973.
[9] H.-S. Kim, B.-W. Cho, W.-I. Cho, J. Power Sources 132 (2004) 235–239.
[10] S.-Y. Chung, J.T. Bloking, Y.-M. Chiang, Nat. Mater. 1 (2002) 123–128.
[11] Y. Wang, G. Cao, Adv. Mater. 20 (2008) 2251–2269.
[12] B. Wang, Y. Qiu, L. Yang, Electrochem. Commun. 8 (2006) 1801–1805.
[13] N.J. Yun, H.-W. Ha, K.H. Jeong, H.-Y. Park, K. Kim, J. Power Sources 160 (2006) 1361–1368.
[14] K.-F. Hsu, S.-Y. Tsay, B.-J. Hwang, J. Mater. Chem. 14 (2004) 2690–2695.
[15] M.-R. Yang, T.-H. Teng, S.-H. Wu, J. Power Sources 159 (2006) 307–311.
[16] Y. Zhou, J. Wang, Y. Hu, R. OaHayre, Z. Shao, Chem. Commun. 46 (2010) 7151–7153.
[17] Y.S. Hu, Y.G. Guo, R. Dominko, M. Gaberscek, J. Jamnik, J. Maier, Adv. Mater. 19 (2007) 1963–1966.
[18] F. Croce, A.D. Epifanio, J. Hassoun, A. Deptula, T. Olczac, B. Scrosati, Electrochem. Solid-State Lett. 5 (2002) A47–A50.
[19] K.S. Park, S.B. Schougaard, J.B. Goodenough, Adv. Mater. 19 (2007) 848–851.
[20] Y. Wang, Y. Wang, E. Hosono, K. Wang, H. Zhou, Angew. Chem. Int. Ed. 47 (2008) 7461–7465.
[21] C. Delacourt, P. Poizot, S. Levasseur, C. Masquelier, Electrochem. Solid-State Lett. 9 (2006) A352–A355.
[22] Y. Ding, Y. Jiang, F. Xu, J. Yin, H. Ren, Q. Zhuo, Z. Long, P. Zhang, Electrochem. Commun. 12 (2010) 10–13.
[23] L. Wang, H. Wang, Z. Liu, C. Xiao, S. Dong, P. Han, Z. Zhang, X. Zhang, C. Bi, G. Cui, Solid State Ionics 181 (2010) 1685–1689.
[24] X. Zhou, F. Wang, Y. Zhu, Z. Liu, J. Mater. Chem. 21 (2011) 3353–3358.
[25] S. Park, J. An, R.D. Piner, I. Jung, D. Yang, A. Velamakanni, S.T. Nguyen, R.S. Ruoff, Chem. Mater. 20 (2008) 6592–6594.
[26] V.H. Nguyen, W.L. Wang, E.M. Jin, H.-B. Gu, J. Alloys Compd. 569 (2013) 29–34.

[27] Z. Fan, K. Wang, T. Wei, J. Yan, L. Song, B. Shao, Carbon 48 (2010) 1686.
[28] D. Yang, A. Velamakanni, G. Bozoklu, S. Park, M. Stoller, R.D. Piner, S. Stankovich, I. Jung, D.A. Field, C.A. Ventrice Jr., R.S. Ruoff, Carbon 47 (1) (2009) 145–152.
[29] Monshi, et al., World J. Nano Sci. Eng. 2 (2012) 154.
[30] S. Park, J. An, I. Jung, R.D. Piner, S.J. An, X. Li, A. Velamakanni, R.S. Ruoff, Nano Lett. 9 (2009) 1593–1597.
[31] Z.G. Lu, M.F. Lo, C.Y. Chung, J. Phys. Chem. C 112 (2008) 7069–7078.
[32] J. Koenig, F. Tuinstra, J. Chem. Phys. 53 (1970) 1126–1130.
[33] S. Stankovich, D.A. Dikin, R.D. Piner, K.A. Kohlhaas, A. Kleinhammes, Y. Jia, Y. Wu, S.T. Nguyen, R.S. Ruoff, Carbon 45 (2007) 1558–1565.
[34] G. Wang, H. Liu, J. Liu, S. Qiao, G.M. Lu, P. Munroe, H. Ahn, Adv. Mater. 22 (2010) 4944–4948.
[35] S.J. Gregg, K.S.W. Sing, Adsorption, Surface Area, and Porosity, Academic Press, London, 1976.
[36] F. Yu, J.-J. Zhang, Y.-F. Yang, G.-Z. Song, J. Mater. Chem. 19 (2009) 9121–9125.
[37] C.M. Doherty, R.A. Caruso, B.M. Smarsly, P. Adelhelm, C.J. Drummond, Chem. Mater. 21 (2009) 5300–5306.
[38] X.-L. Wu, L.-Y. Jiang, F.-F. Cao, Y.-G. Guo, L.-J. Wan, Adv. Mater. 21 (2009) 2710–2714.
[39] C. Sun, S. Rajasekhara, J.B. Goodenough, F. Zhou, J. Am. Chem. Soc. 133 (2011) 2132–2135.
[40] H.-W. Ha, N.J. Yun, K. Kim, Electrochim. Acta 52 (2007) 3236–3241.
[41] F. Nobili, F. Croce, B. Scrosati, R. Marassi, Chem. Mater. 13 (2001) 1642–1646.
[42] Appl. Surf. Sci. 282 (2013) 444–449. J. Alloys Compd. 569 (2013) 29–34.